

Article

Open Access



Boosted thermopower in aqueous thermocells through additives-induced ionic regulation for low-grade heat harvesting

Yijie Mu¹, Kedi Li², Kaiyu Mu³, Yung-Kang Peng², Shien-Ping Feng^{1*}

¹Department of Systems Engineering, City University of Hong Kong, Hong Kong 999077, China.

²Department of Chemistry, City University of Hong Kong, Hong Kong 999077, China.

³Doctech HK Limited, Hong Kong Science Park, Hong Kong 999077, China.

*Correspondence to: Prof. Shien-Ping Feng, Department of Systems Engineering, City University of Hong Kong, Tat Chee Avenue, Kowloon, Hong Kong 999077, China. E-mail: tony.feng@cityu.edu.hk

How to cite this article: Mu, Y.; Li, K.; Mu, K.; Peng, Y. K.; Feng, S. P. Boosted thermopower in aqueous thermocells through additives-induced ionic regulation for low-grade heat harvesting. *Energy Mater.* 2025, 5, 500119. <https://dx.doi.org/10.20517/energymater.2025.34>

Received: 12 Feb 2025 **First Decision:** 26 Mar 2025 **Revised:** 24 Apr 2025 **Accepted:** 30 Apr 2025 **Published:** 12 Jun 2025

Academic Editor: Yizhong Huang **Copy Editor:** Ping Zhang **Production Editor:** Ping Zhang

Abstract

Aqueous thermocells are promising techniques for the conversion of low-grade waste heat into electricity. However, current improvement strategies are mainly focused on single redox ions and sacrifice the electrical conductivity due to concentrated molecular additives. Herein, we report a chemical additives-regulated thermocell that introduced two ionic additives, guanidine hydrochloride and cysteamine hydrochloride, into 0.4 M ferri/ferrocyanide $\{[\text{Fe}(\text{CN})_6]^{3-/4-}\}$ electrolyte to simultaneously exert the selective crystallization effect on $[\text{Fe}(\text{CN})_6]^{4-}$ and the chemical regulation effect for $[\text{Fe}(\text{CN})_6]^{3-}$, synergistically inducing concentration gradients of both redox ions between two electrodes, thereby improving the thermoelectric performance. Our thermocell obtained a high thermopower of 4.34 mV K^{-1} with comparable electrical conductivity and a Carnot-relative efficiency of 5.50% with minimal amounts of the two additives, showing adaptability to various cell orientations and thus different practical scenarios. A record-high thermopower of 9.06 mV K^{-1} and a Carnot-relative efficiency of 12.65% were achieved by adopting optimized concentrations of two additives under cold-over-hot orientation. A 20-unit module was developed to directly power various electronics, demonstrating its feasibility for low-grade heat harvesting.

Keywords: Thermocells, guanidine hydrochloride, cysteamine hydrochloride, chemical regulation



© The Author(s) 2025. **Open Access** This article is licensed under a Creative Commons Attribution 4.0 International License (<https://creativecommons.org/licenses/by/4.0/>), which permits unrestricted use, sharing, adaptation, distribution and reproduction in any medium or format, for any purpose, even commercially, as long as you give appropriate credit to the original author(s) and the source, provide a link to the Creative Commons license, and indicate if changes were made.



INTRODUCTION

Low-grade heat ($< 100\text{ }^{\circ}\text{C}$) is an abundant energy source, spreading over a variety of natural and industrial processes, such as solar and geothermal energy, the human body, transportation, *etc.*^[1,2]. Recovery of low-grade heat, such as converting it into electricity, is a promising way to deal with energy-related crisis. Various technologies have been proposed for the thermal-electrical energy conversion. Conventional solid-state thermoelectric cells based on the Seebeck effect employ electrons and holes in semiconductors or semimetals as charge carriers for direct conversion between heat and electricity. In addition, molecular thermoelectrics also offer nanoscale material design strategies for thermal energy conversion^[3-5]. However, within the temperature range of the low-grade heat, the applications of traditional thermoelectric materials are hindered by relatively low thermoelectric response and high cost of rare raw materials, which can only generate thermopower (S , also known as Seebeck coefficient) in the magnitude of $\mu\text{V K}^{-1}$ ^[6-8]. An alternative approach is liquid-state thermogalvanic cells (or thermocells). For thermoelectric materials, electrons or holes are the charge carriers, which can pass through the electrode end to generate current^[9-11]. In contrast, ions are the charge carriers in thermocells, experiencing redox reactions with electron transfer at two electrodes under different temperatures, and cannot pass into the electrodes. With ions as charge carriers, thermocells enable high thermopower generation in the order of mV K^{-1} within the low-temperature range via the thermogalvanic effect, that is, the temperature-dependent electrode potential of redox couple^[12-14]. Benefiting from the high thermoelectric response, thermocells have been widely applied in fields of body heat-powered technologies and disaster alarm systems, such as fire warning systems^[15,16].

For thermocell systems, thermopower is the thermovoltage generated under a temperature difference (ΔT), which is associated with the solvent-dependent entropy difference (ΔS) between redox ions and the concentration difference (ΔC) of redox ions between hot and cold electrodes^[17,18]. In other words, thermopower can be enhanced by increasing ΔS of the redox ions or introducing ΔC . A higher ΔS can be realized by regulating the interactions between the redox ions and the solvents, such as a rearrangement of the solvation shell by adopting organic redox couples or additives^[19-24]. In a 0.4 M ferri/ferrocyanide $\{[\text{Fe}(\text{CN})_6]^{3-/4-}\}$ electrolyte system, chaotropic guanidinium chloride and polar urea were employed as additives to obtain a thermopower of 4.2 mV K^{-1} . However, the electrical conductivity of the system ($\sim 5\text{ S m}^{-1}$) and the mass transport of the redox couple were largely decreased due to the concentrated molecular additives of urea ($\sim 24\text{ M}$) introduced and the resulting elevated viscosity, hindering further development due to the limited output power density^[25]. From the perspective of establishing ΔC , the inherent nature of thermocell systems exhibiting a tendency toward homogeneity and thermodynamical stability makes it challenging to maintain a permanent ΔC within the electrolytes, which typically decays to near zero via the spontaneous diffusion of redox ions over time^[26-28]. A recent work first managed to establish a continuous ΔC in aqueous $[\text{Fe}(\text{CN})_6]^{3-/4-}$ -based thermocell system by crystallizing $[\text{Fe}(\text{CN})_6]^{4-}$ via guanidinium ions, exhibiting a thermopower of 3.73 mV K^{-1} ^[26]. Nevertheless, the thermopower enhancement might still be limited since guanidinium ions regulate only the behavior of $[\text{Fe}(\text{CN})_6]^{4-}$ rather than both redox ions. In addition, the single crystallization-driven improvement also made the thermocells largely orientation-dependent, rendering them less conducive for practical use.

Herein, we introduced guanidine hydrochloride (GdnHCl) and cysteamine hydrochloride (CH) into 0.4 M $[\text{Fe}(\text{CN})_6]^{3-/4-}$ -based electrolyte, and we label this system a GdnHCl-CH-co-regulated thermocell (GCTC). With minimal amounts of the two additives, GCTC exhibited an enhancement of thermopower from 1.21 mV K^{-1} to 4.34 mV K^{-1} , a higher value than those of current aqueous thermocells, and a Carnot-relative efficiency of 5.50% over the commercialization threshold of 5%, while maintaining a comparable electrical conductivity of the thermocells (25 S m^{-1}). Notably, as required by practical applications, GCTCs also overcome the dependence on cell orientations, allowing for adaptability to

non-unidirectional heat flows. Moreover, the performance was further boosted to record-high values of 9.06 mV K^{-1} and 12.65%, respectively, by optimizing the concentrations of both ionic additives. The joint contribution from the selective crystallization effect between GdnHCl and $[\text{Fe}(\text{CN})_6]^{4-}$ and the chemical regulation effect between CH and $[\text{Fe}(\text{CN})_6]^{3-}$ synergistically alter the concentration profiles of $[\text{Fe}(\text{CN})_6]^{4-}$ and $[\text{Fe}(\text{CN})_6]^{3-}$ ions, accounting for the enhanced thermoelectric performance. A prototyping module comprising 20 units of GCTCs with minimal additives demonstrated its capability of powering various electronics with an open-circuit voltage (V_{oc}) of 4.11 V and a maximum power output (P_{max}) of 25.73 mW under a temperature difference of 50 K. This strategy is proposed to serve as a new design pathway for establishing high-performance aqueous thermocell systems, promoting the development of liquid-state thermocells that better adapt to practical scenarios.

EXPERIMENTAL

Materials

Potassium ferricyanide [$\text{K}_3\text{Fe}(\text{CN})_6$, ACS, $\geq 99.0\%$], potassium ferrocyanide trihydrate [$\text{K}_4\text{Fe}(\text{CN})_6 \cdot 3\text{H}_2\text{O}$, ACS, 98.5%-102.0%], guanidine hydrochloride (GdnHCl, 99.5%), cysteamine hydrochloride (CH, 98%), and cystamine dihydrochloride (CDH, $> 97.0\%$) were purchased from Aladdin Biochemical Technology Co., Ltd. (Shanghai, China). Deuterium oxide (D_2O , 99.9 atom % D) was purchased from MREDA Technology Co., Ltd. (Beijing, China). All chemicals were used as received without further purification. Graphite plates were commercial products purchased from Tailin Graphite Company (Guangdong, China). Water used in all experiments was deionized (DI) water from a Milli-Q ultrapure water purification system (Millipore, France). The Very High Bond (VHB) tape was obtained from 3M (U.S.).

Fabrication of GCTC devices and the integrated module

$\text{K}_3\text{Fe}(\text{CN})_6$ (658.5 mg) and $\text{K}_4\text{Fe}(\text{CN})_6 \cdot 3\text{H}_2\text{O}$ (844.8 mg) were dissolved in DI water to prepare 5 mL of the 0.4 M potassium ferri/ferrocyanide $\{[\text{Fe}(\text{CN})_6]^{3-/4-}\}$ electrolyte as one-cell amount in all experiments. Then a mixture of different molar concentrations of GdnHCl and various mass concentrations of CH were weighed corresponding to the volumetric amount of the pristine $[\text{Fe}(\text{CN})_6]^{3-/4-}$ electrolyte to be added. The GCTC electrolyte was obtained by adding the pristine electrolyte into the mixture of GdnHCl and CH and subsequent magnetic stirring at 300 rpm for 10 min at 70°C until the additives were completely dissolved. As the primary focus of this study, 5 mL of the 0.4 M $[\text{Fe}(\text{CN})_6]^{3-/4-}$ solution was added into a vial containing a mixture of GdnHCl (238.8 mg) and CH (250 mg) to form 0.5 M GdnHCl-50 mg mL^{-1} CH-co-regulated electrolyte. In the case of GCTCs with a high concentration of GdnHCl (e.g., 3.0 M), GdnHCl was first added into the pristine electrolyte, allowing it to fully dissolve, then CH was added into the GdnHCl-contained solution to form the final electrolyte. For GdnHCl-regulated thermocells (GTCs) and CH-regulated thermocells (CTCs), only one additive, either GdnHCl or CH, was dissolved in the pristine electrolyte at the specified concentrations.

The single planar cell was composed of a poly(methyl methacrylate) (PMMA) frame with an internal volume of 3.375 cm^3 ($1.5 \text{ cm} \times 1.5 \text{ cm} \times 1.5 \text{ cm}$), which was sandwiched by two plain graphite plates as electrodes with a thickness of 2 mm without any further modification. The components were sealed using VHB tapes with a thickness of 1.1 mm, which were hollowed out to have a square void with a side length of 1.5 cm and positioned between the PMMA frame and graphite electrodes. The cross-sectional area of the cell was 2.25 cm^2 , and the distance between the two electrodes was 1.72 cm. The homogeneous electrolyte was injected into the planar cell using a syringe immediately after dissolving.

To fabricate the integrated GCTC module, a PMMA frame consisting of 20 individual cells was first sealed by graphite plates with a thickness of 2 mm using the VHB tapes. Then the individual cells were connected

in series by conductive fabric tapes. Conductive silver paste was used to ensure the adhesion between the graphite electrodes and the conductive fabric tapes as well as promoting the electrical contact between them. The cross-sectional area of a single cell was 2.5 cm² (2.5 cm × 1.0 cm), and the distance between the two electrodes was 1.72 cm. Finally, the homogeneous electrolyte was injected into the as-fabricated module for the demonstration.

Characterization and measurements

Thermovoltage and V-I-P measurement

The V_{oc} was recorded by an electrochemical workstation (CHI 660E, Shanghai Chenhua Instrument Corp). The temperature difference between two electrodes of the thermocells was maintained by a homemade temperature acquisition & feedback system employing the LabVIEW program with two thermoelectric modules. Two thermocouples were placed upon and underneath the thermocell to read and record the temperatures at the electrodes, which were processed by the LabVIEW program so that the thermoelectric modules were controlled to reach the input temperature values, providing designated temperature differences toward the two electrodes. The current-voltage curves, employing the same experimental setup as that for thermopower measurement, were obtained by sweeping the voltage from the V_{oc} to 0 V for the cells under the temperature differences. The corresponding power output was acquired by multiplying the current and voltage. For the large-scale module, the temperature difference was created by a hot plate on the bottom, and an aluminum heat exchanger on the top with cooling water circulating through, which was read from a thermometer using K-type thermocouples for temperature sensing.

Electrical conductivity measurement

The electrical conductivity of GCTCs was determined via electrochemical impedance spectroscopy (EIS) conducted on the identical cell configuration and experimental setup as the one for the thermopower measurement, except using Autolab (PGSTAT302N, Metrohm) instead of the electrochemical workstation. The cells were tested under the open circuit condition with a voltage amplitude of 20 mV in the frequency range from 1 to 10⁵ Hz. The resistances were attained via the first intercept of the high frequency on the horizontal axis from Nyquist plots. The electrical conductivity of the thermocells can be calculated as

$$\sigma = l/(R \cdot S) \quad (1)$$

where l is the distance between the two electrodes, R is the resistance, and S is the contact area between the electrolyte and electrode.

Thermal conductivity measurement

The thermal conductivity of the thermocells was measured via a steady-state method. Since there are thermal conduction and thermal convection occurring in the liquid electrolyte in the thermocells under temperature differences, the steady-state method takes both factors into account^[26,29,30]. A planar cell shaped as a rectangular cuboid was composed of two PMMA plates (50 mm × 50 mm × 5 mm) with a thermal conductivity of 0.16 W m⁻¹ K⁻¹, and four polyethylene terephthalate (PET) sheets (50 mm × 15 mm × 0.5 mm). The PMMA plates as the heat transfer walls were placed at the top and bottom sides with a distance of 15 mm, while the bottom side was attached to a thermoelectric module for heating. The PET sheets were employed as the side walls of the cell, which were further covered using thick polystyrene foam to prevent heat transfer between the cell and the surroundings. The electrolyte was injected into the cell. Sufficient time (> 1 h) was applied for the temperature gradient within the cell to reach the steady state. The corresponding equilibrium temperature profiles were recorded by an infrared camera (FLIR SC 660). The software (FLIR QuickReport) was used to process the captured infrared thermography images, indicating

different temperatures across the cell. Based on the conservation of heat flux, the heat flow across the PMMA walls equals that passing through the intermediate electrolyte. Thus, the thermal conductivity can be calculated as

$$\kappa_{\text{bottom wall}} A (\partial T / \partial d)_{\text{bottom wall}} = \kappa_{\text{electrolyte}} A (\partial T / \partial d)_{\text{electrolyte}} = \kappa_{\text{top wall}} A (\partial T / \partial d)_{\text{top wall}} \quad (2)$$

where κ is the thermal conductivity, A is the cross-section area of the cell, and $\partial T / \partial d$ is the temperature change with distance within each component. For our setup, $\kappa_{\text{bottom wall}} = \kappa_{\text{top wall}}$.

Cyclic voltammetry characterization

The cyclic voltammetry (CV) measurements were conducted based on an electrochemical workstation. The three-electrode CV characterizations were conducted using a graphite sheet (size: $1 \times 1 \text{ cm}^2$) as the working electrode, a platinum foil (size: $0.5 \times 2 \text{ cm}^2$) as the counter electrode, and an Ag/AgCl in saturated KCl solution as the reference electrode at a scan rate of 10 mV s^{-1} . The solution for all CV analyses was prepared by adding 15 mL DI water into a mixture of 1 mL 0.4 M $[\text{Fe}(\text{CN})_6]^{4-}$ aqueous solution and 4 mL 2.5 M KCl electrolyte. That is, 0.02 M $[\text{Fe}(\text{CN})_6]^{4-}$ aqueous solution and 0.5 M KCl as the supporting electrolyte were employed. For CV analyses involving GdnHCl and CH, the solution preparation procedures were similar but with sole GdnHCl, sole CH, or both GdnHCl and CH added into the mixture. The temperatures were controlled via a thermostat water bath (SUNNE, SY-DF3-1A) from room temperature to 343 K with each step of an increment of 10 K.

X-ray diffraction characterization

The induced precipitates were retrieved from the thermocells, washed with DI water, and then vacuum dried at 333 K overnight. The pure $\text{K}_3\text{Fe}(\text{CN})_6$, $\text{K}_4\text{Fe}(\text{CN})_6$, GdnHCl, and the dried crystals were ground into powders for the X-ray diffraction (XRD) characterization using the X-ray diffraction system (Rigaku SmartLab SE).

Ultraviolet-visible spectroscopy characterization

The ultraviolet-visible (UV-Vis) absorption spectra were obtained using a UV-Vis spectrophotometer (LAMBDA 365, PerkinElmer). The electrolytes, with or without the additives, were prepared via the same procedure as that for fabricating a thermocell, which were further diluted to have the base $[\text{Fe}(\text{CN})_6]^{3-/4-}$ in a concentration of $1 \times 10^{-4} \text{ M}$.

^1H nuclear magnetic resonance characterization

The evolution of the additives in the pristine electrolyte was tracked using the nuclear magnetic resonance (NMR) system (Bruker ASCEND AVANCE III, 400 MHz). The mass concentration of CH was fixed at 20 mg mL^{-1} .

RESULTS AND DISCUSSION

Thermopower of GTCs

The effect of different concentrations of a single additive, GdnHCl or CH [Supplementary Figure 1A and B], on the thermopower of the thermocells was first investigated. The thermocell, which exclusively incorporates different molar concentrations of GdnHCl ($x \text{ M}$) and different mass concentrations of CH ($y \text{ mg mL}^{-1}$) as the additives, is named $x \text{ M-GTC}$ and $y \text{ mg mL}^{-1}\text{-CTC}$, respectively. Figure 1A and B present the thermopower of GTCs and CTCs with different concentrations of the additives based on the same cell configuration and experimental setup [Supplementary Figure 1C and D], respectively. The thermopower of thermocell containing pristine electrolyte, 0.4 M $[\text{Fe}(\text{CN})_6]^{3-/4-}$ without any additives, was 1.21 mV K^{-1} . As

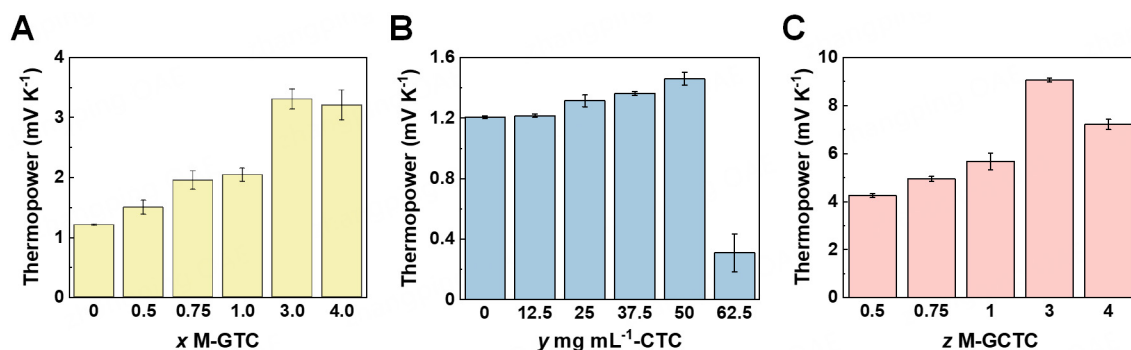


Figure 1. Thermopower of the thermocell systems. (A) GTCs with different molar concentrations of GdnHCl (x M-GTCs); (B) CTCs with different mass concentrations of CH (y mg mL⁻¹-CTCs); (C) GCTCs with 50 mg mL⁻¹ CH and different molar concentrations of GdnHCl (z M-GCTCs). Error bars represent the standard deviation of repeated measurements under the same experimental conditions. GTCs: GdnHCl-regulated thermocells; CTCs: CH-regulated thermocells; GCTCs: GdnHCl-CH-co-regulated thermocells.

the molar concentration of GdnHCl additive increased in GTCs, the thermopower reached a maximum value of 3.31 mV K⁻¹ at x of 3.0 M (3.0 M-GTC). This trend is consistent with the one reported in the literature^[26]. While there was only CH as the additive in the pristine electrolyte, the thermopower showed a marginal increase with the rising concentrations of CH in CTCs. The maximum thermopower was 1.46 mV K⁻¹ when y was 50 mg mL⁻¹ (50 mg mL⁻¹-CTC). Surprisingly, we discovered that remarkably high thermopowers were achieved when GdnHCl and CH were simultaneously introduced into 0.4 M [Fe(CN)₆]^{3-/4-} electrolyte. The mass concentration of CH in GCTCs was fixed at 50 mg mL⁻¹, and thermocells with increasing GdnHCl concentrations (z M) are named z M-GCTCs. As shown in Figure 1C, the thermopower of GCTCs with increasing GdnHCl concentrations presented a similar pattern to that of GTCs. For 0.5 M-GCTC, the thermopower was enhanced to 4.34 mV K⁻¹. This high thermopower surpasses values previously reported for aqueous thermocells.^[24-26] When both additives were at their optimal concentrations, that is, 3.0 M GdnHCl and 50 mg mL⁻¹ CH, an extremely high thermopower of 9.06 mV K⁻¹ was obtained in 3.0 M-GCTC. It appears that there is a synergistic contribution toward the thermopower enhancement in the [Fe(CN)₆]^{3-/4-}-based thermocells with CH and GdnHCl addition.

Working mechanism of GCTCs

Upon observation, we noted that there were crystals forming at the top cold electrode (~293 K), which subsequently fell to the bottom hot electrode due to gravity and then dissolved gradually. As shown in Supplementary Figure 2, after the addition of GdnHCl, a slight shift was detected in the absorption peak of [Fe(CN)₆]⁴⁻ electrolyte in the UV-Vis spectra, while the one for [Fe(CN)₆]³⁻ remained unchanged with GdnHCl additive compared with those of pristine electrolyte. It reveals that the interaction induced by GdnHCl is specifically with [Fe(CN)₆]⁴⁻ rather than [Fe(CN)₆]³⁻ ions. This is attributed to the stronger chaotrope-chaotrope interaction between guanidine cations and [Fe(CN)₆]⁴⁻ than [Fe(CN)₆]³⁻ ions, and the [Fe(CN)₆]⁴⁻-related crystals have been confirmed to possess high thermosensitive solubility^[25,26,31,32]. Additionally, we retrieved the precipitates accumulated at the hot electrode from GCTCs for X-ray powder diffraction characterization [Supplementary Figure 3]. The peaks of GdnHCl-induced crystals in GCTCs were consistent with those reported^[26,31,32]. These results indicate that the precipitates are formed via the crystallization of [Fe(CN)₆]⁴⁻ ions induced by GdnHCl, and it is a new species different from [Fe(CN)₆]⁴⁻ and GdnHCl. Hence, the addition of GdnHCl can induce the crystallization of [Fe(CN)₆]⁴⁻ ions, thus regulating the [Fe(CN)₆]⁴⁻ concentration profile in GCTCs. A different result is presented in terms of adding CH into the [Fe(CN)₆]^{3-/4-} electrolyte. As illustrated in the UV-Vis spectra in Figure 2A, the characteristic absorption peak of [Fe(CN)₆]⁴⁻ electrolyte barely changed after CH was added. By contrast, the absorption peak for [Fe(CN)₆]³⁻ electrolyte exhibited no substantial change upon the initial addition of CH, but the characteristic

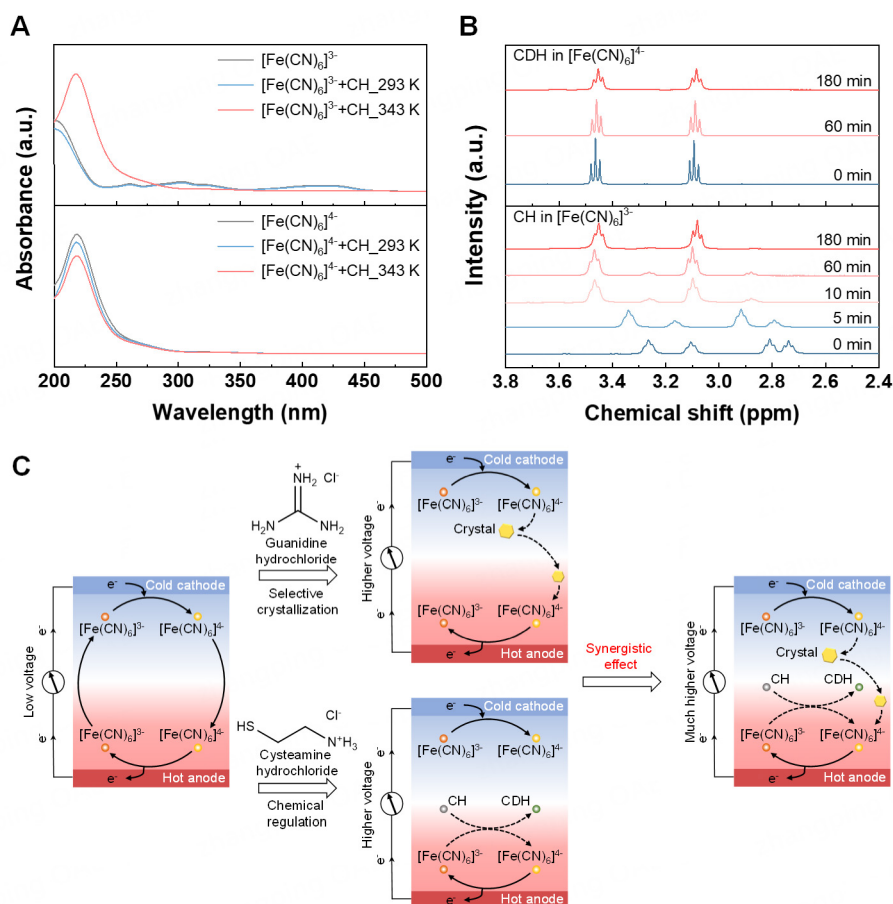


Figure 2. Working mechanism of the thermopower enhancement in GdnHCl-CH-co-regulated thermocells (GCTCs). (A) UV-Vis absorption spectra of $[\text{Fe}(\text{CN})_6]^{4-}$ and $[\text{Fe}(\text{CN})_6]^{3-}$ with 50 mg mL⁻¹ CH as the additive at 293 K and 343 K, respectively; (B) ¹H NMR spectra tracking the evolution of CH dissolved in D₂O-based $[\text{Fe}(\text{CN})_6]^{3-}$ electrolyte upon heating at 343 K, and ¹H NMR spectra of the solution of CDH in D₂O-based $[\text{Fe}(\text{CN})_6]^{4-}$ electrolyte at 343 K over time; (C) Schematic operation mechanism of thermocells with the additives of GdnHCl and CH. UV-Vis: Ultraviolet-visible; NMR: nuclear magnetic resonance.

peak of $[\text{Fe}(\text{CN})_6]^{4-}$ appeared and that of $[\text{Fe}(\text{CN})_6]^{3-}$ weakened significantly after the solution was heated at 343 K, confirming the interaction of CH with $[\text{Fe}(\text{CN})_6]^{3-}$ instead of $[\text{Fe}(\text{CN})_6]^{4-}$ ions occurs as temperature rises, which results in the generation of $[\text{Fe}(\text{CN})_6]^{4-}$. CV analysis was further implemented to validate this chemical interaction between CH and $[\text{Fe}(\text{CN})_6]^{3-}$ ions. As shown in [Supplementary Figure 4A](#), for the pristine electrolyte, as the scan approached the oxidation peak, the current was dictated by the diffusion of $[\text{Fe}(\text{CN})_6]^{4-}$ ions from the bulk electrolyte to the electrode where the oxidation reaction from $[\text{Fe}(\text{CN})_6]^{4-}$ to $[\text{Fe}(\text{CN})_6]^{3-}$ occurred. The diffusion layer, the solution volume containing oxidized $[\text{Fe}(\text{CN})_6]^{3-}$ at the electrode surface, kept growing and gradually slowed down the ionic transport of $[\text{Fe}(\text{CN})_6]^{4-}$ to the electrode. When the potential was scanned negatively, according to the Nernst equation, $[\text{Fe}(\text{CN})_6]^{3-}$ at the electrode surface was reduced back to $[\text{Fe}(\text{CN})_6]^{4-}$. As given in [Supplementary Figure 4B](#), no redox peaks were observed for aqueous CH itself within the scan potential window at varying temperatures. [Supplementary Figure 4C-E](#) illustrate the voltammetric responses of aqueous $[\text{Fe}(\text{CN})_6]^{4-}$ with the additives of sole CH, sole GdnHCl, and both GdnHCl and CH, respectively. It was obvious that, when CH was added into $[\text{Fe}(\text{CN})_6]^{4-}$ electrolyte, the reduction peak referred to the reduction of $[\text{Fe}(\text{CN})_6]^{3-}$ to $[\text{Fe}(\text{CN})_6]^{4-}$ was weakened, and the oxidation peak corresponding to the oxidation of $[\text{Fe}(\text{CN})_6]^{4-}$ to $[\text{Fe}(\text{CN})_6]^{3-}$ was strengthened with increasing temperatures. On the contrary, there was no evident change in the redox

peaks in the CV curves after GdnHCl was solely introduced into $[\text{Fe}(\text{CN})_6]^{4-}$ electrolyte. The redox peaks in the electrolyte of $[\text{Fe}(\text{CN})_6]^{4-}$ with GdnHCl and CH showed an analogous trend to those for CH in $[\text{Fe}(\text{CN})_6]^{4-}$ electrolyte, that is, the reduction peak was diminished, while the oxidation peak was enhanced. These results imply that the diffusion of redox ions and the corresponding electron transfer at the electrode under elevated temperatures are partly affected by the introduction of CH additive in the GCTC system. The homogeneous interaction at the hot electrode between CH and $[\text{Fe}(\text{CN})_6]^{3-}$ caused the partial depletion of $[\text{Fe}(\text{CN})_6]^{3-}$, causing a certain impact on reversibility.^[33] The CV analysis further substantiates that the reaction between $[\text{Fe}(\text{CN})_6]^{3-}$ and CH occurs with elevated temperatures and then generates $[\text{Fe}(\text{CN})_6]^{4-}$.

^1H NMR spectroscopy (400 MHz, D_2O) was employed to further reveal the underlying mechanism. [Supplementary Figure 5A](#) shows the ^1H NMR spectra for a solution of CH dissolved in D_2O . There were only two triplets with an intensity ratio of 1:1 at 3.16 ppm and 2.79 ppm observed. The peaks are attributed to the two groups of hydrogen atoms in two $-\text{CH}_2-$ adjacent to $-\text{SH}$ and $-\text{NH}_3^+$, respectively^[34]. Additionally, CH possesses relative thermal stability in aqueous solution during the specified period, as the peaks in the ^1H NMR spectrum showed no distinct shift after the solution was heated at 343 K for 180 min. Comparable findings were noted for CH dissolved in D_2O -based $[\text{Fe}(\text{CN})_6]^{4-}$ electrolyte, which further demonstrates that CH has no interaction with $[\text{Fe}(\text{CN})_6]^{4-}$ and stably exists in $[\text{Fe}(\text{CN})_6]^{4-}$ when subjected to heat [[Supplementary Figure 5B](#)]. As presented in [Figure 2B](#), when CH was added into D_2O -based $[\text{Fe}(\text{CN})_6]^{3-}$ solution and heated at 343 K from 0 (initial dissolution at room temperature $\sim 24^\circ\text{C}$) to 180 min, at the shortest time upon dissolution, the ^1H NMR spectrum for $[\text{Fe}(\text{CN})_6]^{3-}$ solution already showed some unexpected species different from the ones in the solution of CH in D_2O without $[\text{Fe}(\text{CN})_6]^{3-}$, emphasizing the presence of some signals that appear to correlate with intermediate species, which exist only at the initial stage after the solute is added into the solvent. However, the evolution of CH in $[\text{Fe}(\text{CN})_6]^{3-}$ electrolyte upon heating gradually became clear when the heating time was over 10 min. Two distinctive triplets at 3.45 ppm and 3.08 ppm were detected to have an intensity ratio between them close to 1:1 after heating for 180 min. With the evidence of $[\text{Fe}(\text{CN})_6]^{4-}$ being one of the products from the interaction between CH and $[\text{Fe}(\text{CN})_6]^{3-}$, we found that the signals from the end product tracked in the evolution of CH in $[\text{Fe}(\text{CN})_6]^{3-}$ solution upon heating were correlated with those identified in the ^1H NMR spectra of CDH dissolved in D_2O -based $[\text{Fe}(\text{CN})_6]^{4-}$, which presented two characteristic triplet peaks with an intensity ratio of 1:1 at 3.45 and 3.08 ppm, respectively. Moreover, it is worth noting that CDH exhibits thermal stability upon heating at 343 K within the prescribed timeframe for no obvious shifts detected. The result reveals that the generation of CDH, a dimer consisting of two deprotonated CH ions, via the interaction between CH and $[\text{Fe}(\text{CN})_6]^{3-}$. Accordingly, we deduce the interaction between $[\text{Fe}(\text{CN})_6]^{3-}$ and CH in our thermocell system as below:



Analogous to the interaction between $[\text{Fe}(\text{CN})_6]^{3-}$ and cysteine, we propose that there are two possible mechanistic pathways for the oxidation of CH to CDH [[Supplementary Figure 6](#)]. In route one, the deprotonation of CH occurs prior to the oxidation reaction, and then the corresponding radicals are generated^[35,36]. The second route begins with direct oxidation of the protonated CH, generating a thiol radical cation intermediate that undergoes deprotonation to form a radical species, which produces CDH through the coupling process^[37]. Both transformation routes of CH are believed to participate in the chemical interaction with $[\text{Fe}(\text{CN})_6]^{3-}$ ions. In other words, the oxidation of CH to CDH involves the initial generation of the thiyl radicals and the subsequent evolution into CDH as the product.

As depicted in [Figure 2C](#), the chaotropic GdnHCl selectively induces the crystallization of $[\text{Fe}(\text{CN})_6]^{4-}$ at the cold electrode, resulting in a low concentration of $[\text{Fe}(\text{CN})_6]^{4-}$ at the cold side. Thus, the reduction reaction

from $[\text{Fe}(\text{CN})_6]^{3-}$ to $[\text{Fe}(\text{CN})_6]^{4-}$ by obtaining one electron from the electrode is enhanced, and the local concentration of $[\text{Fe}(\text{CN})_6]^{3-}$ decreases as well. Then, driven by the gravity force, the crystals precipitate onto the bottom hot electrode, and redissolve at the hot electrode due to the thermosensitivity, resulting in a high concentration of $[\text{Fe}(\text{CN})_6]^{4-}$ at the hot side. With the release of $[\text{Fe}(\text{CN})_6]^{4-}$, the oxidation reaction from $[\text{Fe}(\text{CN})_6]^{4-}$ to $[\text{Fe}(\text{CN})_6]^{3-}$ by transferring one electron to the electrode is enhanced, leading to an increasing local concentration of $[\text{Fe}(\text{CN})_6]^{3-}$. The $[\text{Fe}(\text{CN})_6]^{3-}$ -sensitive CH interacts with $[\text{Fe}(\text{CN})_6]^{3-}$ ions at the hot electrode, rendering the concentration of $[\text{Fe}(\text{CN})_6]^{3-}$ to reduce. The electrocatalytic reduction of $[\text{Fe}(\text{CN})_6]^{3-}$ back to $[\text{Fe}(\text{CN})_6]^{4-}$, which can be reoxidized, increases the concentration of $[\text{Fe}(\text{CN})_6]^{4-}$ at the hot electrode simultaneously. When both additives, GdnHCl and CH, are introduced into the electrolyte, a low local concentration of $[\text{Fe}(\text{CN})_6]^{4-}$ near the cold side enhances the reduction reaction from $[\text{Fe}(\text{CN})_6]^{3-}$ to $[\text{Fe}(\text{CN})_6]^{4-}$ with more electrons attracted from the cold electrode to the electrolyte, while a high local concentration of $[\text{Fe}(\text{CN})_6]^{4-}$ and a low local concentration of $[\text{Fe}(\text{CN})_6]^{3-}$ near the hot side favor the oxidation reaction from $[\text{Fe}(\text{CN})_6]^{4-}$ to $[\text{Fe}(\text{CN})_6]^{3-}$ with more electrons transferred from the electrolyte to the hot electrode. As a result, the thermopower of GCTCs is enhanced due to the regulated ΔC of both redox ions along with the improved ΔS [Supplementary Note 1].

With regard to the reaction between CH and $[\text{Fe}(\text{CN})_6]^{3-}$, an excessive amount of CH in the electrolyte may lead to instant depletion of the redox ions, which is detrimental to the thermocell system, exhibiting the sharp decline of thermopower in CTCs with CH over 50 mg mL^{-1} . In other words, for CH, a mass concentration of 50 mg mL^{-1} guarantees both the operation of the thermocells and the thermopower enhancement. Since CH at its optimal concentration exhibited only a slight improvement in the thermopower in CTCs compared to the enhancement effect induced via the two additives of GdnHCl and CH in GCTCs, we infer that the addition of GdnHCl in GCTCs not only contributes to the establishment of $[\text{Fe}(\text{CN})_6]^{4-}$ concentration gradient via the selective crystallization effect between two electrodes, but also facilitates the chemical regulation interaction of CH and $[\text{Fe}(\text{CN})_6]^{3-}$, enhancing its reaction kinetics. Therefore, when CH is added into the pristine electrolyte alone, the co-existence of the redox couple impedes the reaction kinetics between CH and $[\text{Fe}(\text{CN})_6]^{3-}$, thus the thermopower enhancement contributed by the chemical regulation effect is not fully manifested and the value is relatively low. Once GdnHCl is added together with CH, the crystallization of $[\text{Fe}(\text{CN})_6]^{4-}$ by GdnHCl leaves more $[\text{Fe}(\text{CN})_6]^{3-}$ to interact with CH in the liquid phase. Thus the chemical regulation effect between CH and $[\text{Fe}(\text{CN})_6]^{3-}$ is fully exerted. The two effects synergistically enhance the thermopower, generating a notably high thermopower. The electrolyte of $[\text{Fe}(\text{CN})_6]^{3-}$ with sole CH additive dissolved at 343 K is displayed in Supplementary Figure 7A, manifesting clear green color when CH directly interacts with $[\text{Fe}(\text{CN})_6]^{3-}$. Supplementary Figure 7B-F presents the comparison of color evolution of the $[\text{Fe}(\text{CN})_6]^{3-/4-}$ electrolytes with both GdnHCl and CH additives (left) and with CH as the exclusive additive (right) over time. The left one with both GdnHCl and CH as the chemical additives also showed a clear green color similar to that of sole CH in $[\text{Fe}(\text{CN})_6]^{3-}$, which provides direct visual evidence confirming that the addition of GdnHCl to induce the crystallization of $[\text{Fe}(\text{CN})_6]^{4-}$ allows CH to better interact with $[\text{Fe}(\text{CN})_6]^{3-}$, synergistically regulating the concentration gradients of the redox couple.

Thermoelectric performance of GCTCs

Comprehensive analyses were performed in terms of the thermoelectric properties of GCTCs. We measured the electrical conductivity in the presence of varying temperature differences using EIS [Supplementary Figure 8]. It was found that no visible semicircles were detected in the Nyquist plots of the thermocell systems with/without the additives, which implies that, for both the pristine electrolyte and the electrolyte with two additives, the electron transfer processes between the redox ions and electrodes at the interfaces are rapid^[38,39]. The resistance was obtained via the intersection point with the x -axis in the Nyquist plot. The non-isothermal electrical conductivity of 0.5 M-GCTC increased from 14 S m^{-1} to 25 S m^{-1} with elevated

temperature differences from 0 K to 50 K, which showed a similar trend to that for the pristine thermocell without any additives. The thermal conductivity of 0.5 M-GCTC was obtained via the steady-state method [Supplementary Figure 9], which was $0.314 \text{ W m}^{-1} \text{ K}^{-1}$. Figure 3A presents the power outputs of the thermocells, the pristine, 0.5 M-GTC, 50 mg mL⁻¹-CTC and 0.5 M-GCTC, at a temperature difference of 50 K. Both the thermovoltage and current density exhibited significant improvement for 0.5 M-GCTC, and a $P_{\max}/(\Delta T)^2$ of $3.09 \text{ mW m}^{-2} \text{ K}^{-2}$ was achieved, which was over eight times that of the pristine thermocell of $0.36 \text{ mW m}^{-2} \text{ K}^{-2}$. Additionally, as one of the most important parameters used for evaluating the performance of thermocells, the energy conversion efficiency of our 0.5 M-GCTC yielded a Carnot-relative efficiency (η_{cr}) of 5.50% at a temperature difference of 50 K, which exceeds the commercialization threshold of 5% for thermocell systems, rendering it commercially viable [Supplementary Note 2]^[40]. Furthermore, we also presented the thermoelectric performance of our 3.0 M-GCTC [Supplementary Figure 10]. With a high thermopower of 9.06 mV K^{-1} , a remarkably high η_{cr} of 12.65% was achieved with a more suppressed thermal conductivity of $0.273 \text{ W m}^{-1} \text{ K}^{-1}$ due to a large amount of precipitates near the bottom electrode. It is worth noting that, when it comes to the thermoelectric performance comparison, there are no clear criteria outlining the parameters and conditions involved, making it challenging to evaluate if the optimization method is effective or not. In this work, we proposed the comparison of thermoelectric performance from three perspectives, that is, electrolyte optimization, electrode optimization, and co-optimization of electrolyte and electrode. As shown in Figure 3B and Supplementary Table 1, our GCTCs, focusing on electrolyte modification, outperform other thermocells with optimized electrolytes documented in the literature^[25,26,38,41-45]. Considering the similarities and differences in the thermoelectric performance analysis, such as thermopower, electrical conductivity and thermal conductivity, from traditional thermoelectric materials, a comparison on the widely used methodologies is presented in Supplementary Table 2^[9,24,26,42,44,46-49].

In the aforementioned analyses, the thermocells were placed in a cold-over-hot mode; that is, the electrode on the top of the thermocells was maintained at 293 K, while the bottom electrode was subjected to increasing temperatures with each step of 10 K until reaching 343 K. However, in practical scenarios, the temperature gradient does not consistently exhibit a unidirectional pattern. For example, the ground temperature is typically higher than the air temperature during sunny daytime, whereas the temperature profile reverses during the night period. Supplementary Figure 11 illustrates the thermopower of $[\text{Fe}(\text{CN})_6]^{3-/4-}$ -thermocells with/without additives in different orientations. The pristine thermocells were generally orientation-independent. Nevertheless, with a high concentration of GdnHCl, both 3.0 M-GTC and 3.0 M-GCTC exhibited high dependence on the cell orientations. The thermopower of 3.0 M-GTC was reduced by 68% after the thermocell was switched from cold-over-hot to hot-over-cold mode. The thermopower of 3.0 M-GCTC even presented a sharp decrease of 78% when a hot-over-cold arrangement was applied. In contrast, 0.5 M-GCTC with less GdnHCl addition only experienced a decline of 25% in the thermopower after being placed in a hot-over-cold configuration. Supplementary Figure 12 presents the explanation on the orientation dependence caused by the introduction of GdnHCl. Since gravity-driven precipitation is the determining factor for achieving the thermosensitive crystallization and redissolution cycle of GdnHCl and the redox ions, GdnHCl-added thermocells exhibit high orientation-dependence, which well explains that the thermocells containing concentrated GdnHCl (e.g., 3 M) in hot-over-cold arrangement demonstrated substantial reduction in their thermoelectric responses. By contrast, 0.5 M-GCTC largely reduces the dosage of GdnHCl additive, thereby the dependence of thermoelectric performance enhancement effect on the cell orientations is correspondingly alleviated, and the thermoelectric performance is ensured by the synergistic enhancement contribution from CH addition despite much less GdnHCl being used. With the two additives introduced into the electrolyte, our 0.5 M-GCTC presented a high thermovoltage generation over a continuous operation of ~60 h, as shown in Supplementary Figure 13. It was found that the thermovoltage showed slight fluctuation. This may result

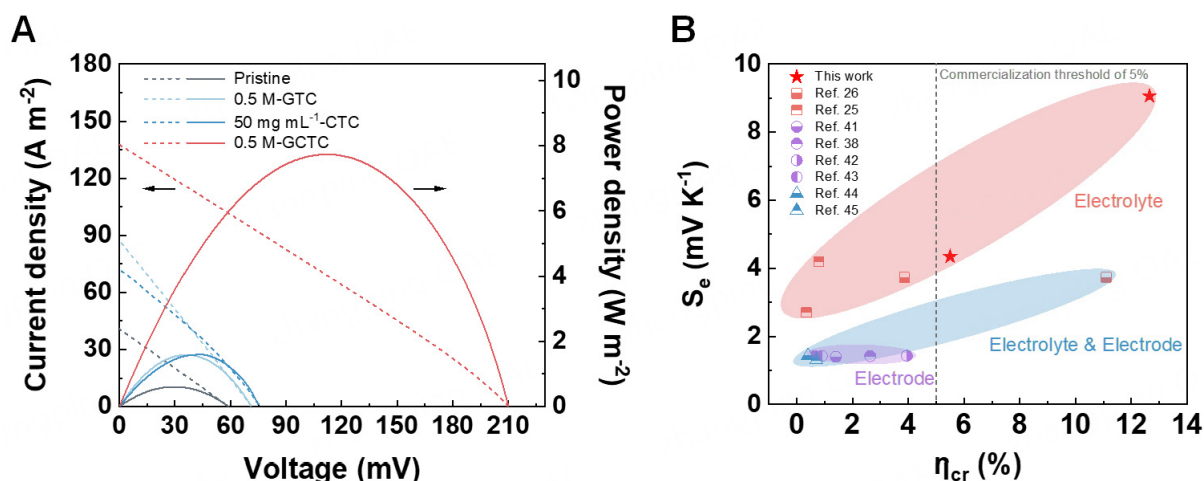


Figure 3. Thermoelectric performance of the thermocells. (A) Current density versus voltage output and corresponding power density of the pristine, 0.5 M-GTC, 50 mg mL⁻¹-CTC, and 0.5 M-GCTC systems at a ΔT of 50 K; (B) Comparison of η_{cr} and S_e values with various $[\text{Fe}(\text{CN})_6]^{3-/4-}$ -based thermocell systems documented in the literature from perspectives of optimization toward electrolyte, electrode, and both electrolyte and electrode, respectively. A dashed line indicates the commercialization threshold of ~5% for thermocells [Supplementary Table 1]. GCTC: GdnHCl-CH-co-regulated thermocell; GTC: GdnHCl-regulated thermocell; CTC: CH-regulated thermocell.

from the difficult precipitation of the crystals and their propensity to adhere to the cold electrode; thus, it took some time for them to gravitationally fall off the cold electrode, which is consistent with the phenomenon that we observed during experiments. Additionally, the crystal layer also causes non-uniformity in the aqueous electrolyte and hinders the electrode accessibility for the redox species^[50,51]. Accordingly, we preferred a low concentration of GdnHCl to be introduced to guarantee the synergistic enhancement effect on the thermopower induced by CH and GdnHCl. Thus, we adopted 0.5 M-GCTCs with 0.5 M GdnHCl and 50 mg mL⁻¹ CH as the additives to demonstrate the potential of our GCTCs for practical applications in low-grade heat harvesting.

Demonstration of integrated GCTC module

A prototype module (size: 185 mm × 70 mm × 15 mm) comprising 20 0.5 M-GCTC units connected in series was designed, as presented in Figure 4A. The as-fabricated module in the cold-over-hot orientation generated an V_{oc} of 4.11 V, a short-circuit current (I_{sc}) of 21.42 mA, and a corresponding P_{max} of 25.73 mW when subjected to a ΔT of 50 K as illustrated in Figure 4B and C. In Figure 4D-F, we demonstrated that our GCTC module was capable of directly powering a series of electronic devices, including an electrochromic smart window, a green light-emitting diode (LED) light and a thermohydrometer [Supplementary Movie 1]. By placing the module in the hot-over-cold mode, a V_{oc} of 3.12 V was generated [Supplementary Figure 14], proving the feasibility of GCTCs for non-unidirectional heat flows. If only the cold-over-hot cell orientation is evaluated in practical scenarios, because of the high thermopower value, we believe that a module consisting of 3.0 M-GCTCs could generate a similar thermovoltage output and power density under the same heat reservoirs with fewer units.

CONCLUSIONS

In summary, a GCTC was prepared by introducing GdnHCl and CH into the 0.4 M $[\text{Fe}(\text{CN})_6]^{3-/4-}$ electrolyte. This strategy, utilizing only small amounts of these two ionic additives, enhances thermopower without compromising electrical conductivity, and is adaptable to different cell orientations. The mechanism was investigated, revealing that thermopower improvement is achieved by regulating the concentration gradients of redox ions between the electrodes based on the thermosensitive crystallization

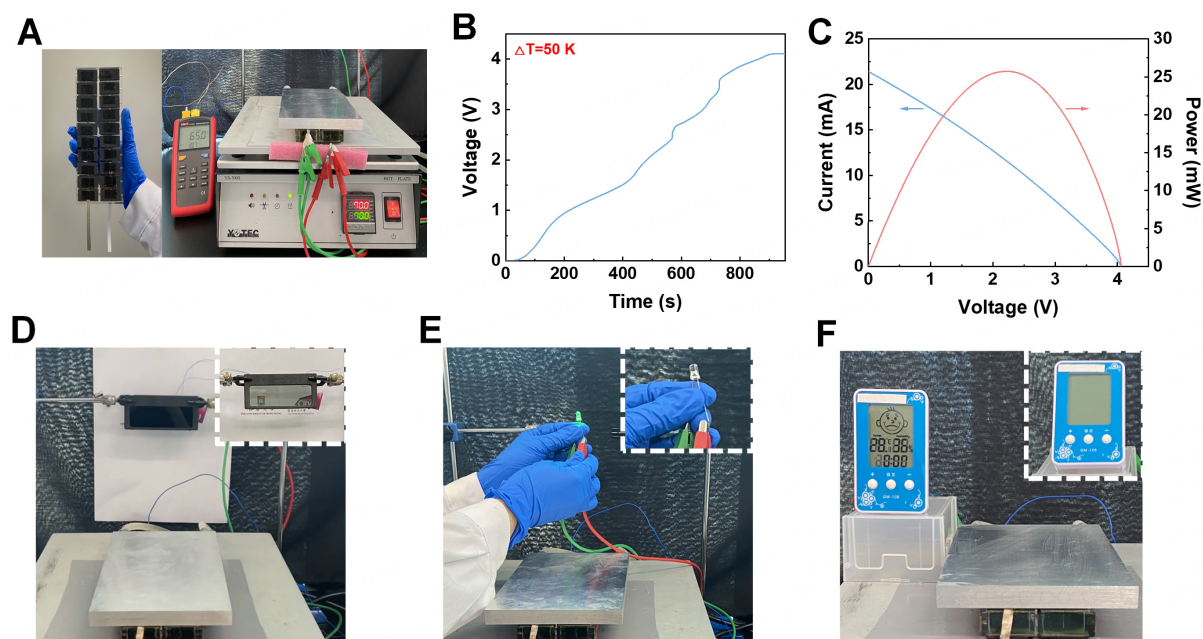


Figure 4. Demonstration of GCTC powering electronic devices. (A) Photographs of a GCTC module containing 20 units of 0.5 M-GCTCs connected in series and the setup for electricity generation; (B) Real-time voltage of the GCTC module under a ΔT of 50 K; (C) Current-voltage curve and corresponding power output of the GCTC module at a ΔT of 50 K; (D-F) Various electronic devices directly powered by the GCTC module, including (D) an electrochromic smart window, (E) a green LED light, and (F) a thermohydrometer. GCTCs: GdnHCl-CH-co-regulated thermocell; LED: light-emitting diode.

effect of GdnHCl on $[\text{Fe}(\text{CN})_6]^{4-}$ and the chemical regulation effect of CH on $[\text{Fe}(\text{CN})_6]^{3-}$. The interaction between GdnHCl and $[\text{Fe}(\text{CN})_6]^{4-}$ also contributes to the reaction kinetics of CH and $[\text{Fe}(\text{CN})_6]^{3-}$, synergistically boosting the thermopower. With low concentrations of the ionic additives, a high thermopower of 4.34 mV K^{-1} was achieved with a satisfactory η_{cr} of 5.50% in the cold-over-hot 0.5 M-GCTC, which could maintain a relatively high value of 3.27 mV K^{-1} when the orientation was reversed. While only considering the cold-over-hot arrangement, the synergistic enhancement could make the performance reach a much higher level of 9.06 mV K^{-1} with a η_{cr} of 12.65% in 3.0 M-GCTC containing a high concentration of GdnHCl. The practical viability was demonstrated via an integrated module with 20 0.5 M-GCTCs configured in series, which generated effective electrical energy to power various electronics, indicating the promising application of our GCTCs for harvesting low-grade heat.

Our work developing the GCTCs aims to provide a new design route for thermocells to improve their thermoelectric performance. Further optimization in the performance of the GCTCs might be achieved by improvement of the reversibility of the interaction between CH and $[\text{Fe}(\text{CN})_6]^{3-}$ via catalysts, modification of the electrode material to improve the current density, adoption of a thermal separator to decrease the thermal conductivity, *etc.*^[44,52,53].

DECLARATIONS

Acknowledgments

The authors would like to acknowledge Dr. Wei-Ting Wang for the design of the thermocell and express their appreciation to Dr. Xun Wang for her assistance in the design and establishment of the thermopower measurement setup.

Authors' contributions

Devised the idea, designed the experiment, interpreted the data, and prepared the manuscript: Mu, Y.; Feng, S. P.

Designed the integrated thermocell module: Mu, Y.; Mu, K.

Performed the experiments and processed the data: Mu, Y.

Conducted the ¹H NMR characterization: Mu, Y.; Li, K.; Peng, Y. K.

Availability of data and materials

The data supporting our findings can be found in the [Supplementary Materials](#).

Financial support and sponsorship

This work was supported by financial support from the General Research Fund (17203520, 17207422) and Collaborative Research Fund (C7082-21G, C6016-22G) from the Research Grants Council of the Hong Kong Special Administrative Region and the Startup Grant of the City University of Hong Kong.

Conflicts of interest

All authors declared that there are no conflicts of interest.

Ethical approval and consent to participate

Not applicable.

Consent for publication

Not applicable.

Copyright

© The Author(s) 2025.

REFERENCES

1. Chu, S.; Majumdar, A. Opportunities and challenges for a sustainable energy future. *Nature* **2012**, *488*, 294-303. [DOI PubMed](#)
2. Gur, I.; Sawyer, K.; Prasher, R. Searching for a better thermal battery. *Science* **2012**, *335*, 1454-5. [DOI PubMed](#)
3. Gemma, A.; Gotsmann, B. A roadmap for molecular thermoelectricity. *Nat. Nanotechnol.* **2021**, *16*, 1299-301. [DOI PubMed](#)
4. He, P.; Jang, J.; Kang, H.; Yoon, H. J. Thermoelectricity in molecular tunnel junctions. *Chem. Rev.* **2025**, *125*, 2953-3004. [DOI](#)
5. Reddy, P.; Jang, S. Y.; Segalman, R. A.; Majumdar, A. Thermoelectricity in molecular junctions. *Science* **2007**, *315*, 1568-71. [DOI PubMed](#)
6. Leblanc, S.; Yee, S. K.; Scullin, M. L.; Dames, C.; Goodson, K. E. Material and manufacturing cost considerations for thermoelectrics. *Renew. Sustain. Energy. Rev.* **2014**, *32*, 313-27. [DOI](#)
7. Hao, F.; Qiu, P.; Tang, Y.; et al. High efficiency Bi₂Te₃-based materials and devices for thermoelectric power generation between 100 and 300 °C. *Energy. Environ. Sci.* **2016**, *9*, 3120-7. [DOI](#)
8. Zhu, B.; Liu, X.; Wang, Q.; et al. Realizing record high performance in n-type Bi₂Te₃-based thermoelectric materials. *Energy. Environ. Sci.* **2020**, *13*, 2106-14. [DOI](#)
9. Zheng, Z.; Shi, X.; Ao, D.; et al. Harvesting waste heat with flexible Bi₂Te₃ thermoelectric thin film. *Nat. Sustain.* **2023**, *6*, 180-91. [DOI](#)
10. Chen, Y. X.; Shi, X. L.; Zhang, J. Z.; et al. Deviceization of high-performance and flexible Ag₂Se films for electronic skin and servo rotation angle control. *Nat. Commun.* **2024**, *15*, 8356. [DOI PubMed PMC](#)
11. Yang, D.; Shi, X. L.; Li, M.; et al. Flexible power generators by Ag₂Se thin films with record-high thermoelectric performance. *Nat. Commun.* **2024**, *15*, 923. [DOI PubMed PMC](#)
12. Dupont, M. F.; MacFarlane, D. R.; Pringle, J. M. Thermo-electrochemical cells for waste heat harvesting - progress and perspectives. *Chem. Commun.* **2017**, *53*, 6288-302. [DOI PubMed](#)
13. Jiao, N.; Abraham, T. J.; Macfarlane, D. R.; Pringle, J. M. Ionic liquid electrolytes for thermal energy harvesting using a cobalt redox couple. *J. Electrochem. Soc.* **2014**, *161*, D3061-5. [DOI](#)
14. Sun, S.; Li, M.; Shi, X.; Chen, Z. Advances in ionic thermoelectrics: from materials to devices. *Adv. Energy. Mater.* **2023**, *13*, 2203692. [DOI](#)
15. Lu, X.; Mo, Z.; Liu, Z.; et al. Robust, efficient, and recoverable thermocells with zwitterion-boosted hydrogel electrolytes for energy-

- autonomous and wearable sensing. *Angew. Chem. Int. Ed.* **2024**, 63, 202405357. DOI
16. Ding, Z.; Du, C.; Long, W.; et al. Thermoelectrics and thermocells for fire warning applications. *Sci. Bull.* **2023**, 68, 3261-77. DOI
 17. Wang, H.; Zhuang, X.; Xie, W.; et al. Thermosensitive-CsI₃-crystal-driven high-power I⁻/I₃⁻ thermocells. *Cell. Rep. Phys. Sci.* **2022**, 3, 100737. DOI
 18. Yu, B.; Xiao, H.; Zeng, Y.; et al. Cost-effective n-type thermocells enabled by thermosensitive crystallizations and 3D multi-structured electrodes. *Nano. Energy* **2022**, 93, 106795. DOI
 19. Abraham, T. J.; Macfarlane, D. R.; Pringle, J. M. High Seebeck coefficient redox ionic liquid electrolytes for thermal energy harvesting. *Energy. Environ. Sci.* **2013**, 6, 2639-45. DOI
 20. Zinovyeva, V.; Nakamae, S.; Bonetti, M.; Roger, M. Enhanced thermoelectric power in ionic liquids. *ChemElectroChem* **2014**, 1, 426-30. DOI
 21. Anari, E. H.; Romano, M.; Teh, W. X.; et al. Substituted ferrocenes and iodine as synergistic thermoelectrochemical heat harvesting redox couples in ionic liquids. *Chem. Commun.* **2016**, 52, 745-8. DOI
 22. Lazar, M. A.; Al-Masri, D.; MacFarlane, D. R.; Pringle, J. M. Enhanced thermal energy harvesting performance of a cobalt redox couple in ionic liquid-solvent mixtures. *Phys. Chem. Chem. Phys.* **2016**, 18, 1404-10. DOI PubMed
 23. Zhou, H.; Yamada, T.; Kimizuka, N. Supramolecular Thermo-electrochemical cells: enhanced thermoelectric performance by host-guest complexation and salt-induced crystallization. *J. Am. Chem. Soc.* **2016**, 138, 10502-7. DOI PubMed
 24. Kim, T.; Lee, J. S.; Lee, G.; et al. High thermopower of ferri/ferrocyanide redox couple in organic-water solutions. *Nano. Energy* **2017**, 31, 160-7. DOI
 25. Duan, J.; Feng, G.; Yu, B.; et al. Aqueous thermogalvanic cells with a high Seebeck coefficient for low-grade heat harvest. *Nat. Commun.* **2018**, 9, 5146. DOI PubMed PMC
 26. Yu, B.; Duan, J.; Cong, H.; et al. Thermosensitive crystallization-boosted liquid thermocells for low-grade heat harvesting. *Science* **2020**, 370, 342-6. DOI
 27. Wang, Y.; Zhang, Y.; Xin, X.; et al. In situ photocatalytically enhanced thermogalvanic cells for electricity and hydrogen production. *Science* **2023**, 381, 291-6. DOI
 28. Yu, B.; Yang, W.; Li, J.; et al. Heat-triggered high-performance thermocells enable a self-powered forest fire alarm. *J. Mater. Chem. A* **2021**, 9, 26119-26. DOI
 29. Kraemer, D.; Chen, G. A simple differential steady-state method to measure the thermal conductivity of solid bulk materials with high accuracy. *Rev. Sci. Instrum.* **2014**, 85, 025108. DOI
 30. Jannot, Y.; Degiovanni, A. Steady-state methods. In *Thermal Properties Measurement of Materials*, 1st ed.; ISTE Ltd and John Wiley & Sons, Inc., 2018; pp 83-116. DOI
 31. Zhang, D.; Mao, Y.; Ye, F.; et al. Stretchable thermogalvanic hydrogel thermocell with record-high specific output power density enabled by ion-induced crystallization. *Energy. Environ. Sci.* **2022**, 15, 2974-82. DOI
 32. Liu, L.; Zhang, D.; Bai, P.; et al. Strong tough thermogalvanic hydrogel thermocell with extraordinarily high thermoelectric performance. *Adv. Mater.* **2023**, 35, e2300696. DOI
 33. Elgrishi, N.; Rountree, K. J.; McCarthy, B. D.; Rountree, E. S.; Eisenhart, T. T.; Dempsey, J. L. A practical beginner's guide to cyclic voltammetry. *J. Chem. Educ.* **2018**, 95, 197-206. DOI
 34. Cui, Y.; Tan, S.; Luo, Z.; et al. Synthesis of cysteamine hydrochloride by high pressure acidolysis of 2-mercaptothiazoline. *Asian. J. Chem.* **2010**, 22, 3221-7. <https://asianpubs.org/index.php/ajchem/article/view/11535> (accessed 2025-06-12).
 35. Dénès, F.; Pichowicz, M.; Povie, G.; Renaud, P. Thiol radicals in organic synthesis. *Chem. Rev.* **2014**, 114, 2587-693. DOI PubMed
 36. Paulsen, C. E.; Carroll, K. S. Cysteine-mediated redox signaling: chemistry, biology, and tools for discovery. *Chem. Rev.* **2013**, 113, 4633-79. DOI PubMed PMC
 37. Nekrassova, O.; Allen, G.; Lawrence, N.; Jiang, L.; Jones, T.; Compton, R. The oxidation of cysteine by aqueous ferricyanide: a kinetic study using boron doped diamond electrode voltammetry. *Electroanalysis* **14**, 1464-9. DOI
 38. Romano, M. S.; Li, N.; Antiohos, D.; et al. Carbon nanotube - reduced graphene oxide composites for thermal energy harvesting applications. *Adv. Mater.* **2013**, 25, 6602-6. DOI
 39. Laschuk, N. O.; Easton, E. B.; Zenkina, O. V. Reducing the resistance for the use of electrochemical impedance spectroscopy analysis in materials chemistry. *RSC. Adv.* **2021**, 11, 27925-36. DOI PubMed PMC
 40. Quickenden, T. I.; Mua, Y. A Review of power generation in aqueous thermogalvanic cells. *J. Electrochem. Soc.* **1995**, 142, 3985. DOI
 41. Hu, R.; Cola, B. A.; Haram, N.; et al. Harvesting waste thermal energy using a carbon-nanotube-based thermo-electrochemical cell. *Nano. Lett.* **2010**, 10, 838-46. DOI
 42. Im, H.; Kim, T.; Song, H.; et al. High-efficiency electrochemical thermal energy harvester using carbon nanotube aerogel sheet electrodes. *Nat. Commun.* **2016**, 7, 10600. DOI PubMed PMC
 43. Qian, W.; Cao, M.; Xie, F.; Dong, C. Thermo-electrochemical cells based on carbon nanotube electrodes by electrophoretic deposition. *Nano-Micro. Lett.* **2016**, 8, 240-6. DOI PubMed PMC
 44. Zhang, L.; Kim, T.; Li, N.; et al. High power density electrochemical thermocells for inexpensively harvesting low-grade thermal energy. *Adv. Mater.* **2017**, 29, 1605652. DOI
 45. Li, G.; Dong, D.; Hong, G.; Yan, L.; Zhang, X.; Song, W. High-Efficiency cryo-thermocells assembled with anisotropic holey graphene aerogel electrodes and a eutectic redox electrolyte. *Adv. Mater.* **2019**, 31, 1901403. DOI

46. Zhao, L. D.; Lo, S. H.; Zhang, Y.; et al. Ultralow thermal conductivity and high thermoelectric figure of merit in SnSe crystals. *Nature* **2014**, 508, 373-7. DOI
47. Burkov, A. T.; Fedotov, A. I.; Novikov, S. V. Methods and apparatus for measuring thermopower and electrical conductivity of thermoelectric materials at high temperatures. In *Thermoelectrics for power generation - a look at trends in the technology*; Skipidarov, S.; Nikitin, M.; Eds.; InTech, 2016; pp 351-87 DOI
48. Wang, H.; Chu, W.; Chen, G. A brief review on measuring methods of thermal conductivity of organic and hybrid thermoelectric materials. *Adv. Elect. Mater.* **2019**, 5, 1900167. DOI
49. Wei, T.; Guan, M.; Yu, J.; Zhu, T.; Chen, L.; Shi, X. How to measure thermoelectric properties reliably. *Joule* **2018**, 2, 2183-8. DOI
50. Jiang, L.; Kirihaara, K.; Nandal, V.; et al. Thermoelectrochemical cells based on ferricyanide/ferrocyanide/guanidinium: application and challenges. *ACS. Appl. Mater. Interfaces*.2022, 22921-8. DOI
51. Zhou, H.; Inoue, H.; Ujita, M.; Yamada, T. Advancement of electrochemical thermoelectric conversion with molecular technology. *Angew. Chem. Int. Ed.* **2023**, 62, e202213449. DOI PubMed
52. Wang, W. T.; Holzhay, P.; Zhou, N.; et al. Water- and heat-activated dynamic passivation for perovskite photovoltaics. *Nature* **2024**, 632, 294-300. DOI
53. Kang, T. J.; Fang, S.; Kozlov, M. E.; et al. Electrical power from nanotube and graphene electrochemical thermal energy harvesters. *Adv. Funct. Mater.* **2012**, 22, 477-89. DOI